ADVANCES IN ATMOSPHERIC SCIENCES, VOL. 26, NO. 5, 2009, 923–939

Cloud Radiative Forcing in Asian Monsoon Region Simulated by IPCC AR4 AMIP Models

LI Jiandong[1,2] (李剑东), LIU Yimin*[1] (刘屹岷), and WU Guoxiong[1] (吴国雄)

[1]*State Key Laboratory of Atmospheric Science and Geophysical Fluid Dynamics (LASG), Institute of Atmospheric Physics, Chinese Academy of Sciences, Beijing* 100029

[2]*Graduate School of Chinese Academy of Sciences, Beijing* 100049

(Received 24 July 2008; revised 19 November 2008)

ABSTRACT

This study examines cloud radiative forcing (CRF) in the Asian monsoon region (0°–50°N, 60°–150°E) simulated by Intergovernmental Panel on Climate Change (IPCC) Fourth Assessment Report (AR4) AMIP models. During boreal winter, no model realistically reproduces the larger long-wave cloud radiative forcing (LWCF) over the Tibet Plateau (TP) and only a couple of models reasonably capture the larger short-wave CRF (SWCF) to the east of the TP. During boreal summer, there are larger biases for central location and intensity of simulated CRF in active convective regions. The CRF biases are closely related to the rainfall biases in the models. Quantitative analysis further indicates that the correlation between simulated CRF and observations are not high, and that the biases and diversity in SWCF are larger than that in LWCF. The annual cycle of simulated CRF over East Asia (0°–50°N, 100°–145°E) is also examined. Though many models capture the basic annual cycle in tropics, strong LWCF and SWCF to the east of the TP beginning in early spring are underestimated by most models. As a whole, GFDL-CM2.1, MPI-ECHAM5, UKMO-HadGAM1, and MIROC3.2 (medres) perform well for CRF simulation in the Asian monsoon region, and the multi-model ensemble (MME) has improved results over the individual simulations. It is suggested that strengthening the physical parameterizations involved over the TP, and improving cumulus convection processes and model experiment design are crucial to CRF simulation in the Asian monsoon region.

Key words: cloud radiative forcing (CRF), AMIP models, Asian monsoon region, Tibet Plateau (TP), active convective region

Citation: Li, J. D., Y. M. Liu, and G. X. Wu, 2009: Cloud radiative forcing in Asian monsoon region simulated by IPCC AR4 AMIP models. *Adv. Atmos. Sci*, **26**(5), 923–939, doi: 10.1007/s00376-009-8111-x.

1. Introduction

Clouds are important modulators of the earth energy budget. Macrophysical and microphysical cloud properties and their distribution have profound impacts on radiative process, precipitation, and the general circulation (Ramanathan et al., 1989; Hartmann et al., 1992). On the global scale, there often exists about 50 percent cloud cover in the sky. Clouds reflect solar radiation back to space and then reduce the radiative flux absorbed by the earth. Meanwhile, clouds trap infrared radiation emitted by the surface and the lower troposphere, which decreases output long-wave radiation (Liou, 2004; Meehl, 2007).

Generally, the concept of cloud radiative forcing (CRF) has been used to quantitatively study the impact of clouds on solar and infrared radiation. CRF at the top of atmosphere (TOA) is defined as the difference between the radiative fluxes with and without clouds (Ramanathan et al., 1989), and includes long-wave CRF (LWCF) and short-wave CRF (SWCF). The relative magnitude between LWCF and SWCF determines the net CRF. Based on the Earth Radiation Budget Experiment (ERBE) data (Barkstrom et al., 1989), many studies have estimated that the global average SWCF and LWCF are approximately -48 W m^{-2} and 31 W m^{-2}, respectively, which leads to a net cloud cooling effect (about -17 W m^{-2}) on

*Corresponding author: LIU Yimin, lym@mail.iap.ac.cn

climate. So, the global annual average SWCF is larger than LWCF. In addition, clouds have significant regional features. In a region, even though the net CRF is close to zero, the cloud effect should not be neglected. Hence, LWCF and SWCF should been investigated separately for a specific study.

Monsoons, which include distinct seasonal variation of the general circulation, temperature, and precipitation, are the dominant climate phenomena over much of Asia (Ding, 1992; Chen et al., 1994; Webster et al., 1998). Cloud physical processes also have distinct features in the Asian monsoon region. Many studies (Kiehl, 1994) have concluded that there is a near cancellation between LWCF and SWCF at the TOA in tropical deep convective regions. Nevertheless, Rajeevan and Srinivasan (2000) argued this conclusion is invalid for the Asian monsoon region, especially for many convective regions, in boreal summer (June, July and August, JJA hereafter), because the net CRF at the TOA is negative and its magnitude exceeds 30 W m^{-2}. Their study also showed that this CRF characteristic is on account of the presence of large amounts of high clouds and the large optical depth of these clouds in these regions. So far, much attention has been paid to CRF in the equatorial Pacific regions. There is lack of extensive research on CRF and its seasonal variation in Asian monsoon region, particularly in the East Asian monsoon region. Meanwhile, due to the complexity of the Asian monsoon system, which has different regional climate characteristics in South Asia, East Asia, and the tropical northwestern Pacific region (Chen et al., 1994; Wang and Lin, 2002). Some studies (Ma and Ji, 2000; Yu et al., 2001) indicated that although both the Indian monsoon region and eastern China belong to the Asian monsoon region and the maximum of precipitation appears in JJA, the properties of clouds and CRF are significantly different. Yu et al. (2004) further showed that the maximum annual mean cloud optical depth between 60°S and 60°N is located on the lee side of the Tibet Plateau (TP), and is produced by persistent deep stratus clouds. These deep stratus clouds are generated and maintained by dynamical effects over the TP and cause extremely strong CRF at the TOA, which fundamentally influences the energy budget in East Asia.

Since the IPCC Third Assessment Report (TAR), the coupled climate models now being used in applications by major climate modeling groups have better performance in simulating seasonally varying patterns of precipitation, mean sea level pressure, and surface air temperature than the models relied on by these same groups at the time of the TAR. However, most current Atmosphere-Ocean General Circulation models (AOGCMs) and Atmospheric General Circulation models (AGCMs) could not simulate the spatial or intra-seasonal variation of monsoon precipitation accurately (Meehl, 2007). Meantime, cloud physics parameterization and its feedback to the climate system remain the largest source of uncertainty in climate simulations, and it is not yet determined which of the model estimates of cloud feedback is the most reliable (Stephens, 2005).

The main motivation of this paper is to examine the performance of current AGCMs for the major features of CRF and its seasonal variation in the Asian monsoon region. Based on IPCC AR4 AMIP models, we evaluate their basic performance in the above aspects, investigate the basic CRF biases of AGCMs, and enhance the understanding of cloud physical process in Asian monsoon region. We also expect this study can supply an important reference for development of AGCMs.

This paper is structured as follows. Section 2 introduces the data and methods used in this analysis. Section 3 qualitatively examines the geographic distribution of CRF simulated by AMIP models in the Asian monsoon region. Section 4 quantitatively evaluates the performance of simulated CRF in the same region. Section 5 analyses the annual cycle of CRF simulated by AMIP models over East Asia. Section 6 provides a discussion and conclusions.

2. Data and methodology

2.1 *Data*

The satellite observational TOA radiative fluxes are taken from ERBE (Barkstrom et al., 1989). The ERBE data consists of monthly mean all-sky and clear-sky radiative fluxes (long-wave and short-wave) at the TOA of 2.5°×2.5° resolution. Uncertainties in the monthly averaged data are estimated to within ±5 W m^{-2}.

The CRF is calculated as follows. The LWCF is defined as

$$\mathrm{LWCF} = F_{\mathrm{clr}} - F \tag{1}$$

where F is the outgoing long-wave radiative flux at the TOA. The subscript "clr" indicates the value in clear-sky conditions. LWCF is usually positive.

The SWCF is defined as

$$\mathrm{SWCF} = S(\alpha_{\mathrm{clr}} - \alpha) \tag{2}$$

where S is the incoming TOA solar flux and α is the total sky albedo of the earth-atmosphere system. Here, α_{clr} is the clear-sky albedo of the earth-atmosphere system. SWCF is usually negative.

CRF depends on not only macrophysical cloud

Table 1. Information about IPCC AR4 AMIP models.

Model	Institute	Resolution(lat×lon)	Reference
CCSM3-CAM3	National Center for Atmospheric Research, USA	T85 (1.4°×1.4°)L26	Collins et al., 2004
CNRM-CM3	Centre National de Recherches Météorologiques, France	T63 (∼1.9°×1.9°)L45	Déqué et al., 1994
GFDL-CM2.1	NOAA/Geophysical Fluid Dynamics Laboratory (GFDL), USA	2.0°×2.5°L24	GFDL GAMDT, 2004
GISS-ER	NASA/Goddard Institute for Space Studies (GISS), USA	4°×5°L20	Schmidt et al., 2006
INM-CM3.0	Institute for Numerical Mathematics, Russia	4°×5°L21	Alekseev et al., 1998; Galin et al., 2003
IPSL-CM4	Institut Pierre Simon Laplace, Paris, France	2.5°×3.75°L19	Hourdin et al., 2006
MIROC3.2 (medres)	CCSR/NIES/FRCGC, Japan	T42 (∼2.8°×2.8°)L20	K-1 Model Developers, 2004
MPI-ECHAM5	Max Planck Institute for Meteorology, Germany	T63 (∼1.9°×1.9°)L31	Roeckner et al., 2003
MRI-CGCM2.3.2	Meteorological Research Institute, Japan	T42L30	Shibata, 1999
UKMO-HadGAM1	Met Office, Hadley Centre, UK	∼1.25°×1.875°L38	Martin et al., 2004

properties including cloud amount and height of the cloud top, but also microphysical cloud properties, such as cloud water path and cloud effective radius. SWCF is also related to incident TOA solar flux (Liou, 2004; Shi, 2007). Using monthly ERBE data spanning 5 years, the climatology and annual cycle of CRF are constructed.

From models participating in IPCC AR4 AMIP, we choose ten models with radiative fluxes in clear-sky conditions and only use their "run1" results. Table 1 lists the names of these models, their development groups, and the resolution, which are supplied by U.S. Department of Energy's Program for Climate Model Diagnosis and Intercomparison (PCMDI). Because of the different simulation periods and horizontal resolution in each model, data from January 1979 to December 1993 was chosen for averaging to construct the climatological CRF for each model. Then the data are interpolated to 2.5°×2.5° boxes just the same as ERBE data. Then, the MME is obtained by arithmetic average of the ten models.

In the present analysis, we also use precipitation and total cloud amount from the ten AMIP models. Additionally, some other observational data used includes the ISCCP (International Satellite Cloud Climatology Project) D1 and D2 datasets (Rossow and Schiffer, 1999) and Climate Prediction Center (CPC) Merged Analysis of Precipitation (CMAP) data (Xie and Arkin, 1997). All of these data are interpolated onto the same grids as ERBE data.

2.2 *Methodology*

In this study, the Asian monsoon region is defined as the domain (0°–50°N, 60°–150°E) (Giorgi and Mearns, 2002; Wang and Lin, 2002; Lau et al., 2006). The spatial patterns of CRF simulated by IPCC AR4 models are validated in the above domain. After that, we examine the annual cycle of CRF around East Asia within the subdomain (0°–50°N, 100°–145°E).

In the following analysis, after the average bias and the root mean squared error (RMSE) are first used to quantitatively assess model biases, a Taylor diagram analysis is applied to evaluate the spatial similarity between models and observations. The Taylor diagram displays three statistics on a 2-D plot citepTaylor01: the variance ratio, correlation coefficient, and the centered RMSE between two fields. The Taylor diagram provides simple and easily interpretable results of a model evaluation or inter-comparison, and can be used to a number of applications (Taylor, 2001). The statistics mentioned above are defined as follows:

$$\overline{E} = \overline{f} - \overline{r} \tag{3}$$

$$E = \left[\frac{1}{N}\sum_{n=1}^{N}(f_n - r_n)^2\right]^{1/2} \tag{4}$$

$$R = \frac{\frac{1}{N}\sum_{n=1}^{N}(f_n - \overline{f})(r_n - \overline{r})}{\sigma_f \sigma_r} \tag{5}$$

$$E' = \left\{\frac{1}{N}\sum_{n=1}^{N}\left[(f_n - \overline{f}) - (r_n - \overline{r})\right]^2\right\}^{1/2} \tag{6}$$

where $\overline{E}$, E, R, and E' are average bias, RMSE, spatial correlation coefficient and centered RMSE, respectively; f_n (r_n) donates the simulation (observation) value at the n-th spatial gridpoint of the climatology, and $\overline{f}$ and $\overline{r}$ are the corresponding area means; $\sigma_{f,r}$

are standard deviations and N is sample number. All of these statistics are calculated as the area-weighted average for each box.

3. Geographic distribution of CRF in Asian monsoon region

3.1 *Geographic distribution of CRF in DJF (December, January, February)*

Figure 1 shows observational cloud radiative properties (CRF, cloud optical depth, TOA albedo, and total cloud) and precipitation in DJF. Strong positive LWCF and negative SWCF are located over the Maritime Continent and tropical western Pacific, where the magnitude of LWCF and SWCF are very close; the maximum LWCF is greater than 70 W m^{-2} and the strongest SWCF is less than -75 W m^{-2}. Meanwhile, the total cloud amount exceeds 75%, corresponding to the large cloud optical depth, TOA albedo, and precipitation in the same region. The LWCF over the TP is 50–60 W m^{-2}, due to higher altitude and temperature at cloud top over the TP (Sun, 1995). Moreover, LWCF is 40–50 W m^{-2} between South Korea and Japan. As shown in Fig. 1, we note that there is very weak LWCF and SWCF between the Indian Peninsula and the Bay of Bengal, where there is weak precipitation, low cloud amount, small cloud optical depth, and low TOA albedo. However, in contrast to weak CRF over South Asia region, strong SWCF appears to the east of the TP, with a magnitude of less than -60 W m^{-2}, which is close to that of the SWCF at the equator. Previous studies (Yu et al., 2001, 2004) indicated that the strong CRF downstream of the TP is mainly correlated with persistent deep stratus clouds with large cloud optical depth and high TOA albedo. These features are also evident in Fig. 1, which shows large cloud albedo and large optical depth.

Figures 2 and 3 show LWCF and SWCF, respectively, from observations and model simulations in DJF. In Fig. 2, four models [GFDL-CM2.1, MIROC3.2 (medres), MRI-CGCM2.3.2 and UKMO-HadGAM1] reproduce the weak LWCF between the

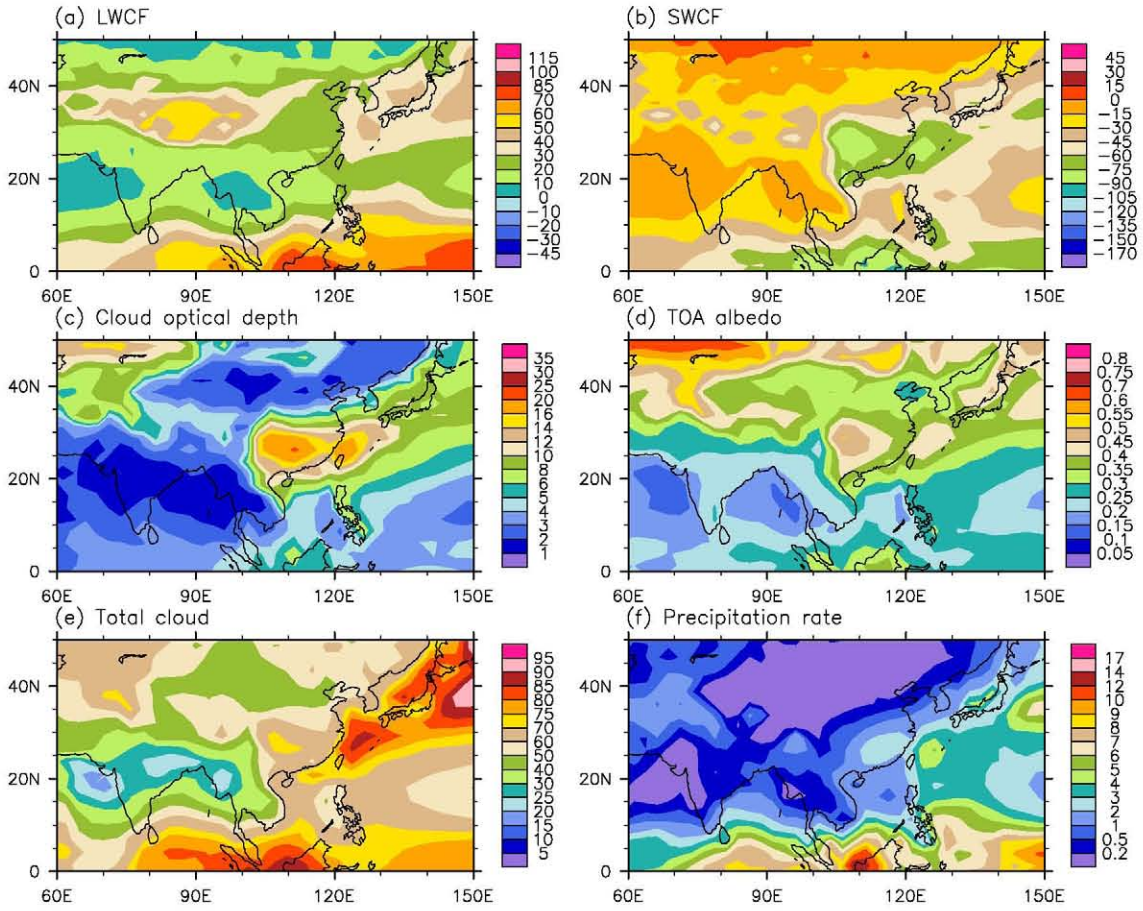

Fig. 1. Geographic distribution of cloud radiative properties for (a) LWCF from ERBE (W m^{-2}), (b) SWCF from ERBE (W m^{-2}), (c) cloud optical depth from ISCCP, (d) TOA albedo from ERBE, (e) total cloud amount (%), and (f) precipitation rate from CMAP (mm d^{-1}) in DJF.

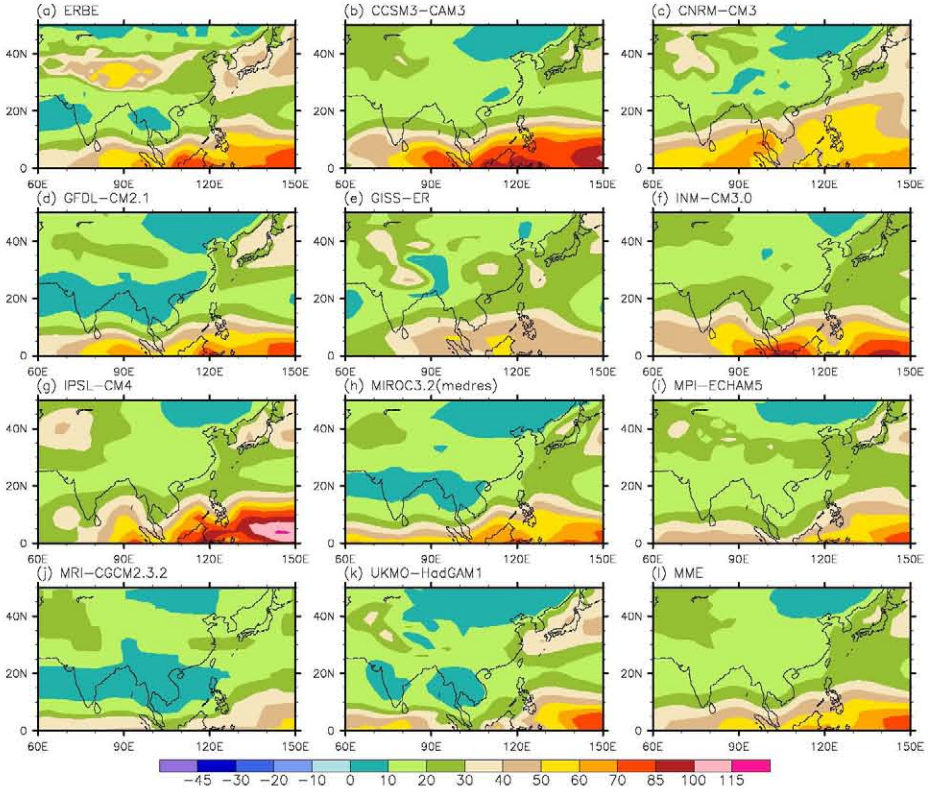

Fig. 2. Geographical distribution of LWCF from (a) ERBE, (b)–(k) IPCC AR4 AMIP models and (l) MME in DJF (units: W m^{-2}).

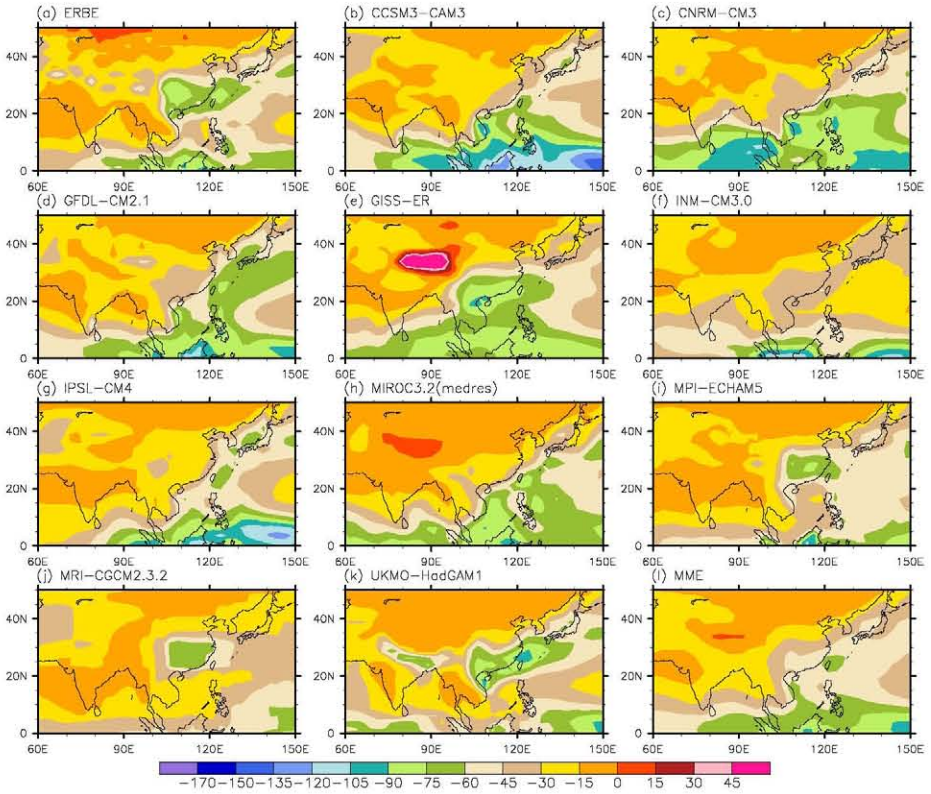

Fig. 3. Same as Fig. 2 except for SWCF.

Indian Peninsula and the Bay of Bengal, but no model captures the strong LWCF over the TP in DJF, which is very likely to be related to complicated land surface and regional cloud physical processes over the TP. Positive LWCF simulated by most of the models is lower than the observation between East China and Japan, which is also shown in the LWCF by the MME result. In tropical regions, most of models capture the strong LWCF.

In Fig. 3, four models (GISS-ER, MPI-ECHAM5, MRI-CGCM2.3.2 and UKMO-HadGAM1) capture the strong SWCF to the east of the TP in DJF. Among the four models, the SWCF from UKMO-HadGAM1 is the closest to the observation. In addition, GFDL-CM2.1 also partly reproduces the SWCF to the east of the TP but the magnitude of SWCF is lower than that of ERBE data. Though the MME underestimates the magnitude of SWCF to the east of the TP, which is caused by the biases of most of models in this region, the MME could basically reproduce the SWCF over most regions in DJF.

3.2 *Geographic distribution of CRF in JJA*

Figure 4 displays the observational cloud radiative features and precipitation in JJA. The CRF is correlated well with strong precipitation in active convective regions. Strong CRF regions are located over the South Indian Peninsula, the Bay of Bengal, and tropical western Pacific, where convection is also strong. As with the strongest rainfall, the strongest CRF also lies in the Bay of Bengal, where LWCF exceeds 85 W m^{-2} and SWCF is less than -120 W m^{-2}. There is also stronger CRF in the Southwest of China. The largest cloud optical depth and TOA albedo are present between the Bay of Bengal and Southwest of China, especially over the Sichuan Basin. In Fig. 4, there are also areas of strong SWCF less than -100 W m^{-2}, corresponding to larger cloud amount, cloud optical depth, and TOA albedo, between the Korean Peninsula and Japan (Raschke et al., 2005).

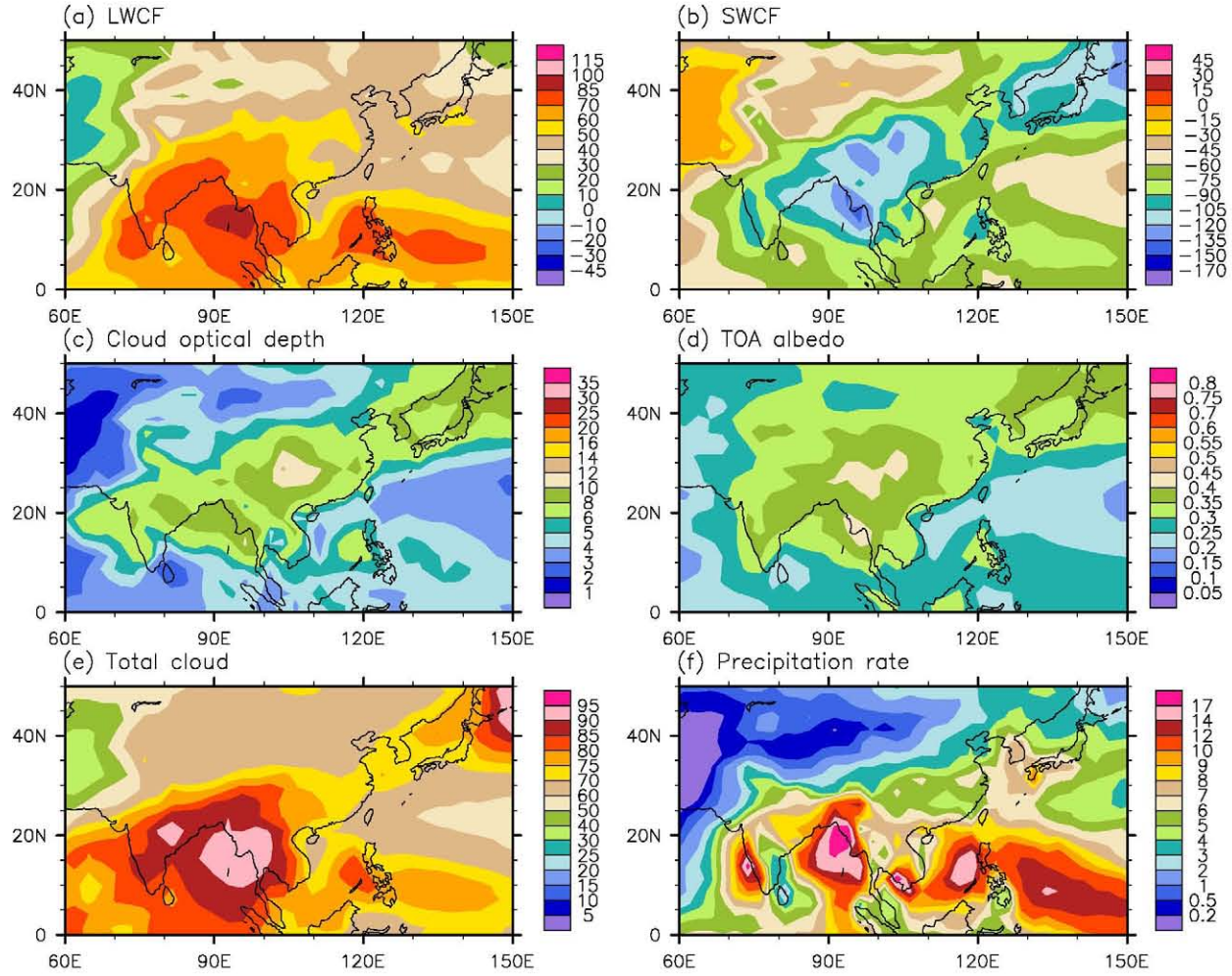

Fig. 4. Same as in Fig. 1 except for JJA.

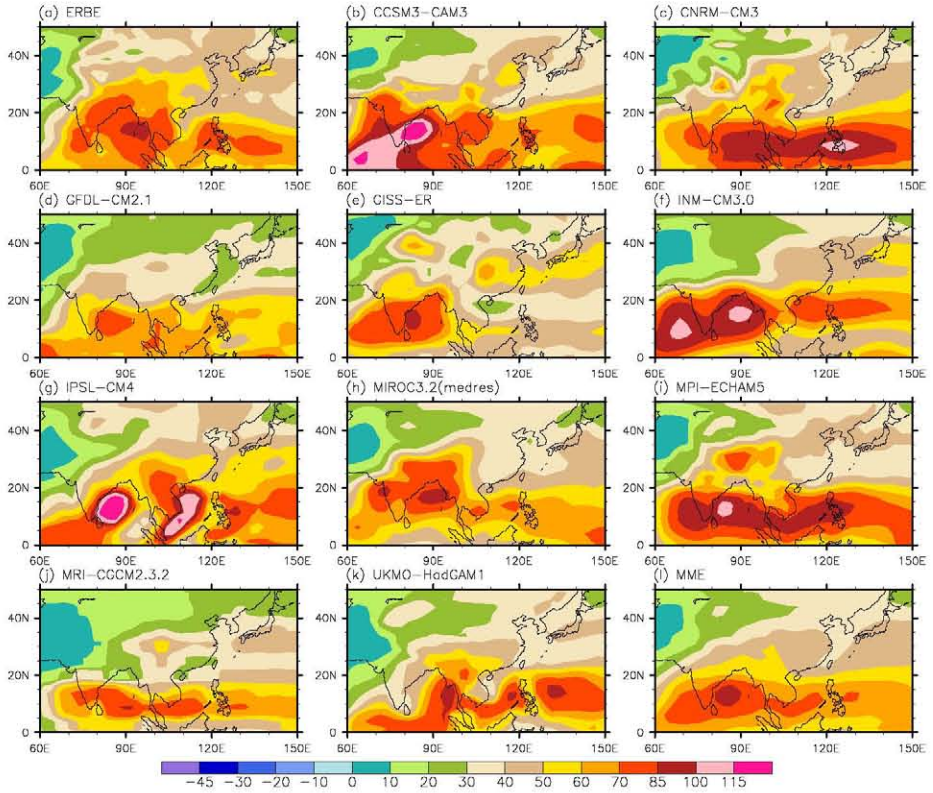

Fig. 5. Geographical distribution of LWCF from (a) ERBE, (b)–(k) IPCC AR4 AMIP models, and (l) MME in JJA (units: W m^{-2}).

Figure 5 and 6 show LWCF and SWCF simulated by AMIP models in JJA, respectively. Most models can reproduce the basic spatial pattern of CRF in the Asian monsoon region, but the simulated location and intensity of LWCF and SWCF have certain biases. In active convective regions, the CRF simulated by AMIP models is correlated well with simulated rainfall (Fig. 7) and are their biases. Most models cannot capture well the strongest LWCF and SWCF over the Bay of Bengal. A similar difficulty for CRF simulation also exists in Southwest China, downstream of the TP, where most models underestimate LWCF and SWCF. In addition, most models have better performance for LWCF and SWCF between the Korean Peninsula and Japan. Similar analysis features are also shown in the MME result.

Referring to Wang and Lin (2002), we choose 3 representative regions as follow: India region (ISM) (5°–20°N, 70°–100°E), western Pacific (WNPSM) (5°–20°N, 110°–140°E) and East Asia (EASM) (20°–35°N, 100°–130°E). Figure 8 shows scatter diagrams between CRF and rainfall in the three regions. Except for several gridpoints, the relationship between observational CRF and rainfall exhibits linear correlation in the tropical ISM and WNPSM regions, where strong CRF just corresponds to strong rainfall. The correlation coefficient between SWCF and rainfall is −0.673 over ISM in JJA, but there is no linear correlation between observational CRF and rainfall to the east of the TP in JJA.

Over ISM and WNPSM, the SWCF simulated by individual AMIP model (figures not shown) and the MME are linearly correlated with rainfall, but the simulations' correlations are much higher than for the observed data. For example, the simulation correlation coefficients between SWCF and rainfall are −0.742 and −0.826 over ISM and WNPSM, respectively, based on the MME. This further indicates that the biases of summer CRF simulated by AMIP models are closely related to the biases of simulated rainfall in active convective regions. It is noted that there are certain linear correlations between CRF, particularly for LWCF, simulated by most models and the rainfall to the east of the TP, a feature which does not agree with the observations.

4. Quantitative validation of CRF in Asian monsoon region

4.1 *Average bias and RMSE*

Table 2 lists average bias and RMSE from AMIP models and observations in DJF and JJA, respectively.

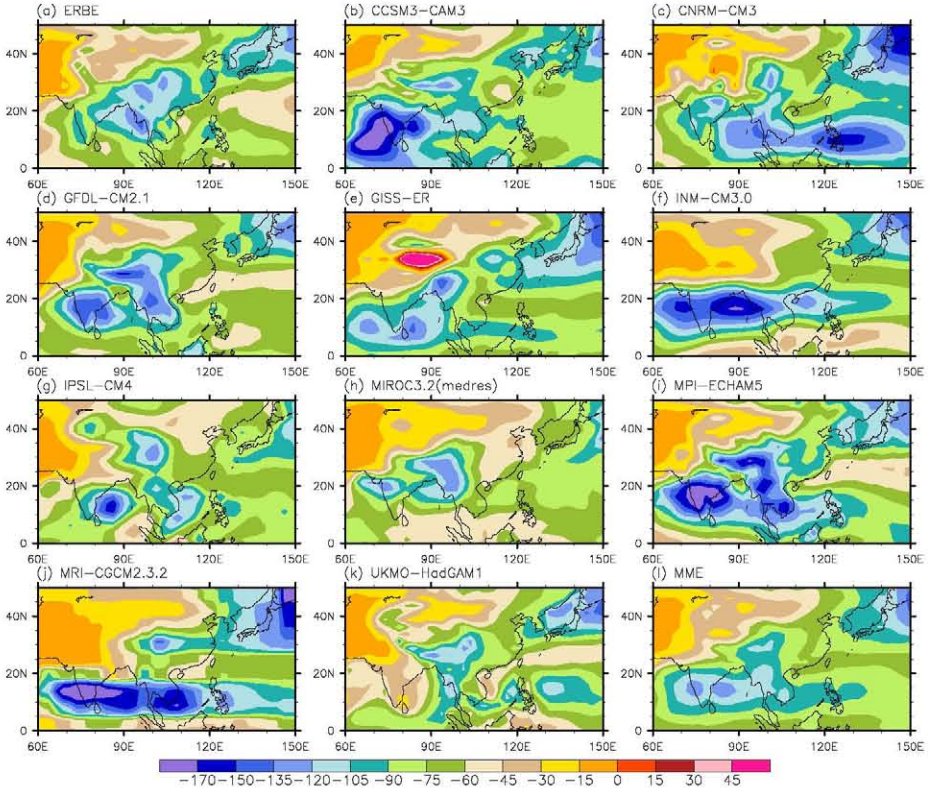

Fig. 6. Same as Fig. 5 except for SWCF.

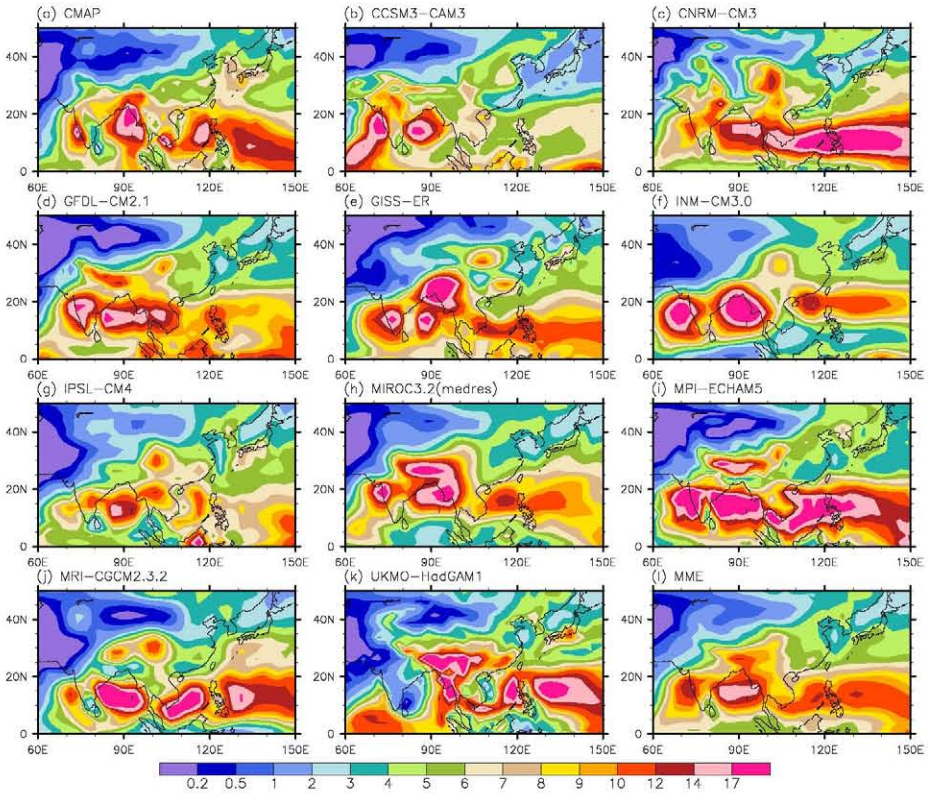

Fig. 7. Geographical distribution of precipitation rate from (a) CMAP, (b)–(k) IPCC AR4 AMIP models, and (l) MME (units: mm d^{-1}).

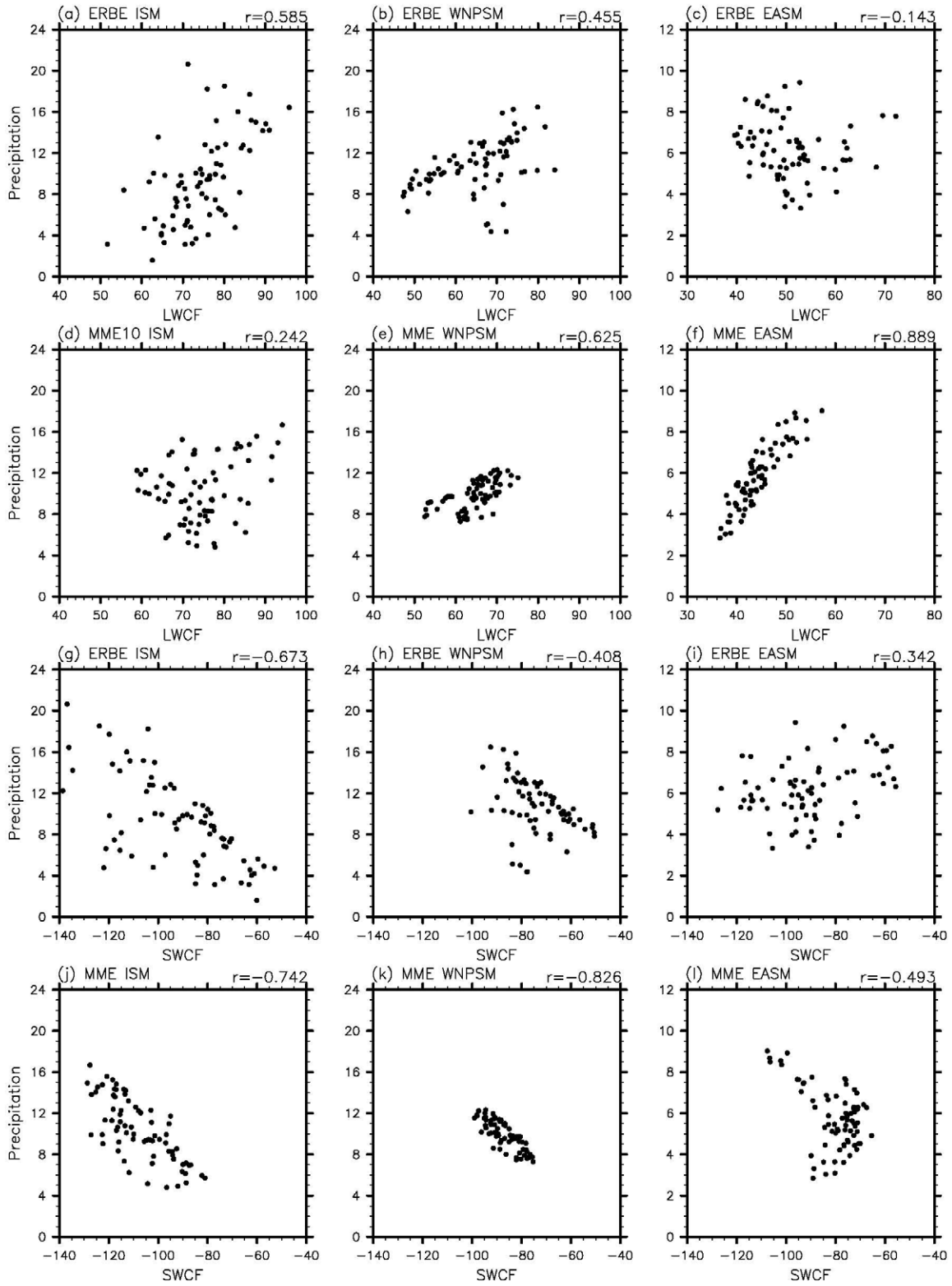

Fig. 8. Scatter diagrams between precipitation and LWCF for (a)–(c) ERBE and (d)–(f) MME in ISM, WNPSM, and EASM in JJA, respectively; (g)–(l) are the same as (a)–(f), except for SWCF. x-axis denotes precipitation (mm d^{-1}) and x-axis denotes corresponding LWCF or SWCF (W m^{-2}). Here, r denotes correlation coefficient.

Table 2. The average bias and RMSE between ERBE and the simulated (and MME) CRF (LWCF and SWCF) over the Asian monsoon region (0°–50°N, 60°–150°E) in DJF and JJA, respectively. In DJF, average of LWCF and SWCF from ERBE are 30.602 and −35.822, respectively. In JJA, average of LWCF and SWCF from ERBE are 51.847 and −71.563, respectively. (units: W m^{-2})

	Average bias				RMSE			
	DJF		JJA		DJF		JJA	
Model	LWCF	SWCF	LWCF	SWCF	LWCF	SWCF	LWCF	SWCF
CCSM3-CAM3	0.732	−10.764	5.036	−16.269	14.207	25.125	18.805	34.563
CNRM-CM3	3.127	−13.18	2.251	−14.037	16.93	27.608	13.84	30.699
GFDL-CM2.1	−7.132	−5.256	−8.781	−3.069	10.97	14.991	13.85	19.068
GISS-ER	−4.823	−5.822	−7.045	−4.258	13.659	23.581	16.787	29.55
INM-CM3.0	−0.347	3.011	0.875	−3.803	13.964	18.204	18.388	30.572
IPSL-CM4	1.451	−1.164	1.253	−0.445	14.689	17.907	17.54	25.755
MIROC3.2(medres)	−7.17	0.376	−2.923	8.072	12.217	19.85	11.073	22.804
MPI-ECHAM5	−5.337	2.957	2.747	−13.708	11.245	11.449	12.911	27.676
MRI-CGCM2.3.2	−13.033	7.451	−13.665	−6.682	17.655	16.401	19.382	38.465
UKMO-HadGAM1	−8.733	1.063	−6.301	4.871	14.484	15.947	14.309	20.565
MME	−3.793	−1.786	−1.975	-5.14	10.709	13.159	9.78	18.193

In DJF, LWCF in most models is weaker than observations, and INM-CM3.0 has the smallest average bias and the largest is from MRI-CGCM2.3.2. The SWCF in different models has large diversity, and the smallest average bias of SWCF is from MIROC3.2 (medres) and the largest from CNRM-CM3. In JJA, the smallest average bias of LWCF is from INM-CM3.0 and the largest is still from MRI-CGCM2.3.2. In Table 2, SWCF in most models is stronger in JJA, and the largest average biases of SWCF are from CCSM3-CAM3, CNRM-CM3, and MPI-ECHAM5, and the smallest is from IPSL-CM4.

In fact, domain averages cannot represent well the regional biases of the simulated CRF. For example, MRI-CGCM2.3.2 which has a large average bias of SWCF successfully reproduces the strong negative SWCF feature to the east of the TP and the weak SWCF in South Asia. Nevertheless, MIROC3.2 (medres), with the smallest average bias of SWCF still cannot capture the SWCF feature to the east of the TP.

To further validate the performance of the models, area-weighed RMSE are used to analyze the CRF. In Table 2, the smallest LWCF RMSE are from GFDL-CM2.1 and MIROC3.2 (medres) in DJF and JJA, respectively, and the largest LWCF RMSE is from MRI-CGCM2.3.2 in both seasons. In DJF, in addition to MPI-ECHAM5 which has the smallest SWCF RMSE, GFDL-CM2.1 also has small SWCF RMSE; the largest SWCF RMSE values are from CNRM-CM3 and CCSM3-CAM3. In JJA, GFDL-CM2.1 has the smallest SWCF RMSE and UKMO-HadGAM1 also has small RMSE; the largest SWCF RMSE is from MRI-CGCM2.3.2. Table 2 also shows that MME has the smallest CRF RMSE in DJF and JJA except that the SWCF RMSE is larger than that of MPI-ECHAM5 in DJF. This suggests that by taking the MME mean, we can reduce the biases between simulations and observations to a substantial degree. Moreover, it is shown in Table 2 that the RMSE of SWCF is larger than that of LWCF, and the RMSE in JJA is larger than that in DJF, which indicates that there exist larger biases of SWCF simulated by IPCC AR4 AMIP, especially in JJA.

4.2 *Taylor diagram analysis*

Figures 9a and 9b are Taylor diagrams for CRF simulated by AMIP models in DJF and JJA, respectively. In a Taylor diagram, the radial distance from the origin represents the standard deviation ratio of simulated CRF to that of observations, and the pattern correlation between two fields is given by the azimuthal position. The nearer to the REF point in a Taylor diagram, the closer the observations to the simulation. In addition, the denseness of points in the diagram donates the magnitude of diversity among different models. A denser distribution of points shows smaller diversity among models and vice versa.

A Taylor diagram analysis is applied to the CRF pattern between observations and AMIP models in order to determine which models are more skillful. Figure 9 represents the result of Taylor diagram analysis for CRF in the Asian monsoon region. As shown in Figs. 9a and 9b, the diversity of SWCF from models is larger than that for LWCF. On the other hand, the diversity of simulated LWCF from different models is also large in DJF, and the LWCF of models are relatively close in JJA. The spatial correlation coeffi-

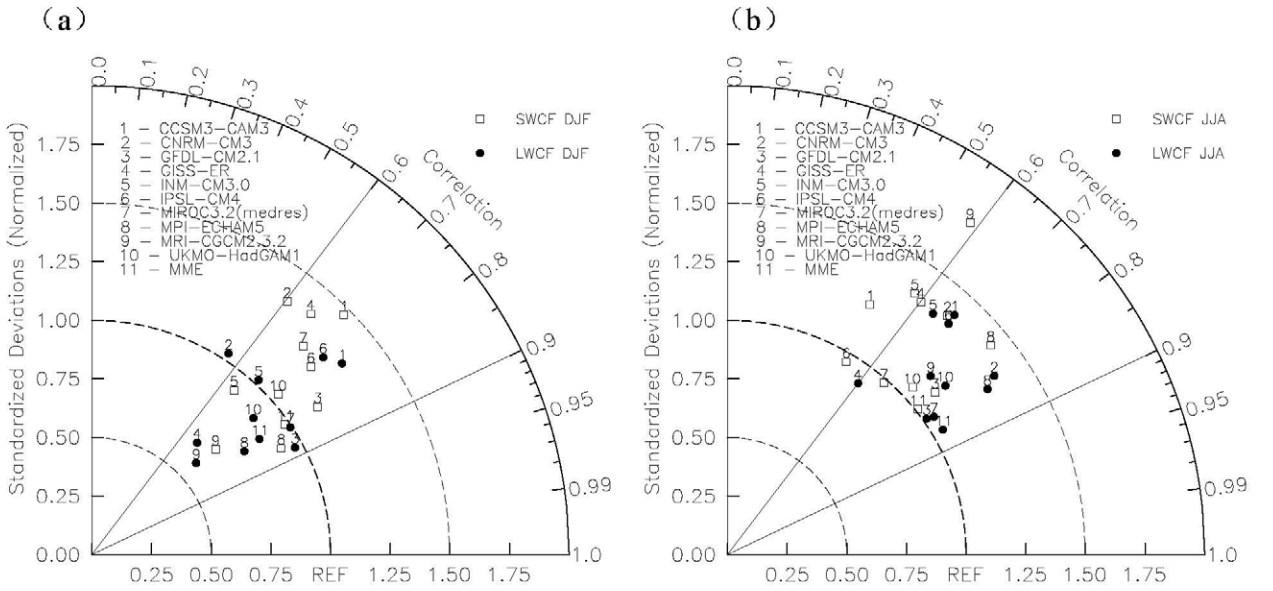

Fig. 9. (a) and (b) are Taylor diagrams for CRF simulated by AMIP models in DJF and JJA, respectively. In a Taylor diagram, the radial distance from the origin represents the standard deviation ratio of simulated CRF to that of observations, and the pattern correlation between two fields is given by the azimuthal position. The nearer to the REF point in a Taylor diagram, the closer the observations to the simulation. In addition, the denseness of points in the diagram donates the magnitude of diversity among different models. A denser distribution of points shows smaller diversity among models and vice versa.

cient between CRF and observations is not high and is less than 0.9. Apart from MPI-ECHAM5, with a correlation coefficient of 0.869 and GFDL-CM2.1 with $r = 0.832$, the spatial correlation coefficient of SWCF in most models is less than 0.8 in DJF, is overall lower than that for LWCF.

In DJF, the Taylor diagram shows that the best performance for LWCF is from GFDL-CM2.1, followed by MIROC2.2 (medres) and MPI-ECHAM5. SWCF from MPI-ECHAM5 has the best performance, and the worst LWCF and SWCF results are from CNRM-CM3.

In JJA, LWCF from GFDL-CM2.1 and MIROC2.2 (medres) have better correlation with observations, and the worst LWCF result is from GISS-ER. SWCF from GFDL-CM2.1 is the closest to observations. At the same time, UKMO-HadGAM1 and MPI-ECHAM5 also have better performance for SWCF, and the worst SWCF result is from CCSM3-CAM3.

Taylor diagrams (Figs. 9a and 9b) further show that CRF in some models, such as LWCF from CNRM-CM3 and SWCF from MRI-CGCM2.3.2, have distinct differences in DJF and JJA. Additionally, some models do not have consistent performance for LWCF and SWCF, such as MIROC2.2 (medres).

In addition to Taylor diagrams, Table 3 shows that GFDL-CM2.1, MPI-ECHAM5, and UKMO-HadGAM1 have better performance for centered RMSE.

Putting together the results of average bias, RMSE, and the Taylor diagram analysis, GFDL-CM2.1, MIROC2.2 (medres), MPI-ECHAM5, and UKMO-HadGAM1 are skillful for CRF simulation out of IPCC AR4 AMIP models. This quantitative conclusion is consistent with geographical distribution analysis. Furthermore, the MME can distinctly reduce the diversity among models and their simulation biases,

Table 3. The normalized centered RMSE for individual IPCC AMIP models and their MME mean over the Asian monsoon region (0°–50°N, 60°–150°E) in DJF and JJA, respectively. The normalized centered RMSE is equal to the standard deviation ratio between the simulated CRF and ERBE.

	DJF		JJA	
Model	LWCF	SWCF	LWCF	SWCF
CCSM3-CAM3	0.817	1.024	1.022	1.14
CNRM-CM3	0.958	1.094	0.771	1.021
GFDL-CM2.1	0.48	0.633	0.602	0.704
GISS-ER	0.735	1.03	0.86	1.093
INM-CM3.0	0.803	0.809	1.036	1.134
IPSL-CM4	0.841	0.806	0.987	0.963
MIROC3.2(medres)	0.569	0.895	0.603	0.797
MPI-ECHAM5	0.57	0.499	0.712	0.899
MRI-CGCM2.3.2	0.685	0.659	0.776	1.416
UKMO-HadGAM1	0.665	0.717	0.725	0.747
MME	0.576	0.588	0.54	0.652

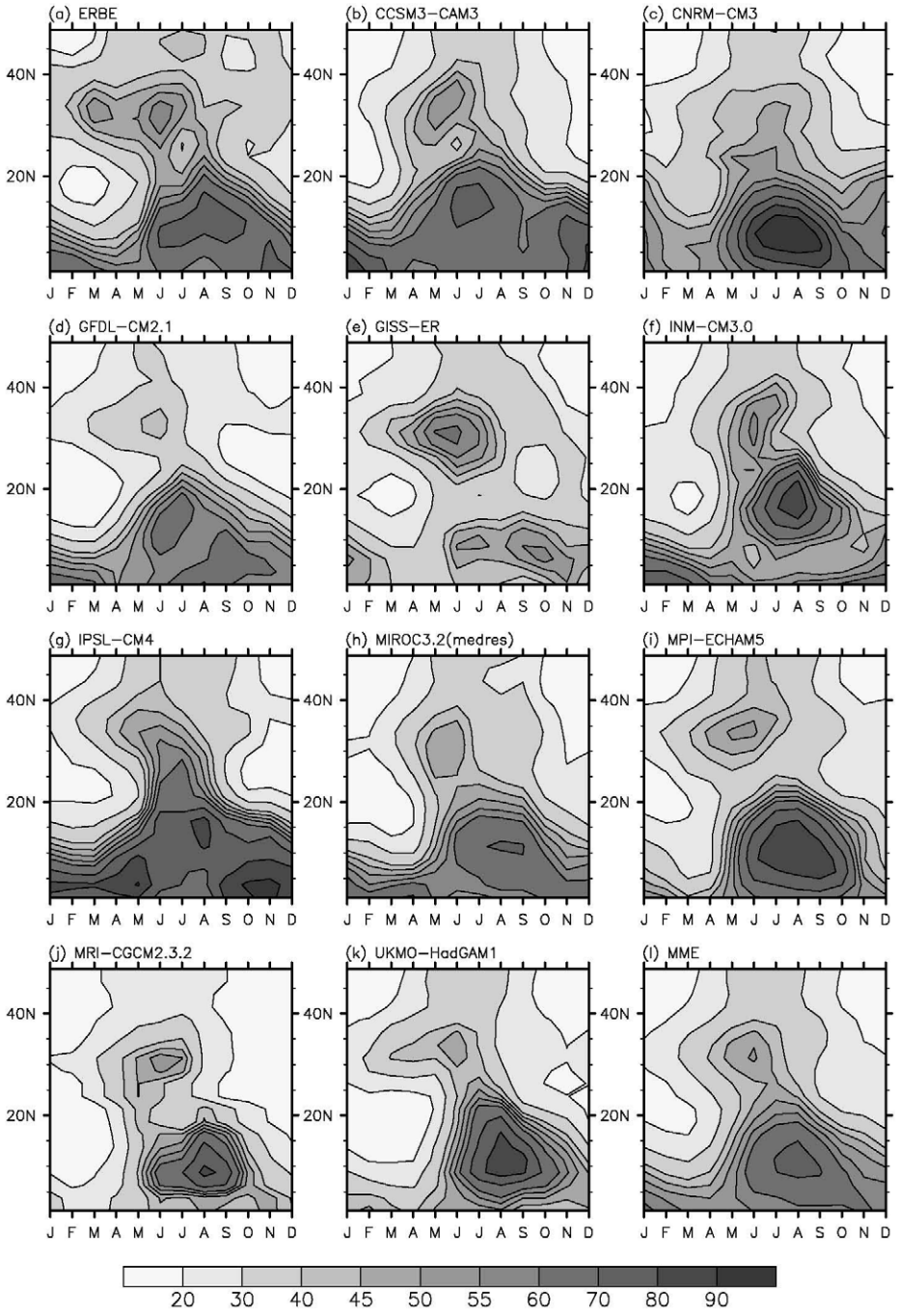

Fig. 10. The annual cycle of LWCF from (a) ERBE, (b)–(k) IPCC AR4 AMIP models, and (l) MME, averaged over 100°–145°E (units: W m^{-2}).

and produce better spatial patterns than most individual models.

5. The annual cycle of CRF over East Asia

The climate features over East Asian are much different from the areas south of that region (Wang and Lin, 2002), and there is strong CRF to the east of the TP in both DJF and JJA. So Figs. 10 and 11 show the observed and simulated annual cycles of LWCF and SWCF near East Asia (0°–50°N and 100°–145°E, including East Asia, the South China Sea, and the tropical western Pacific).

In Figs. 10a and 11a, there are two belts with different features of CRF in these regions. One belt is located to the south of 20°N including the South

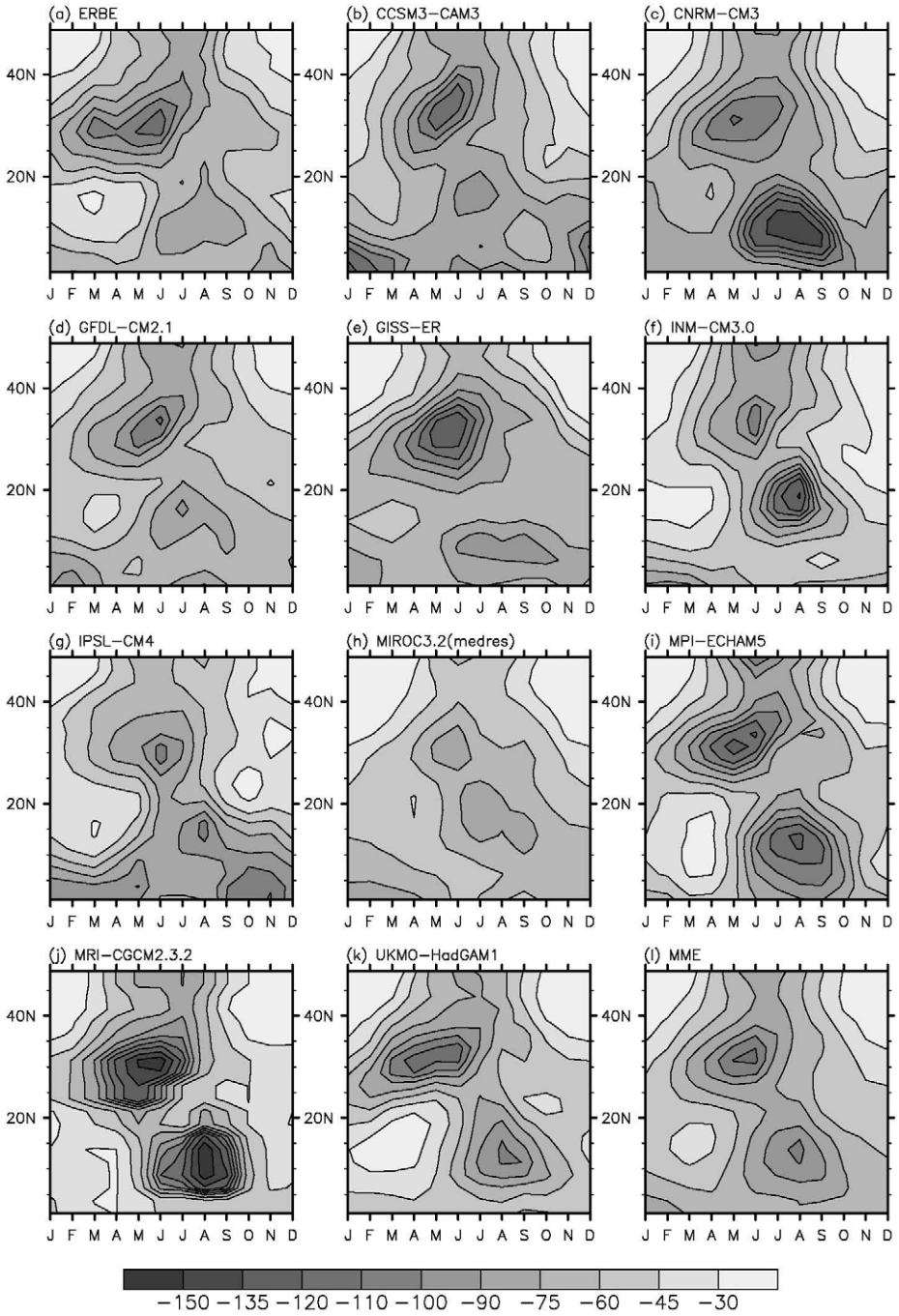

Fig. 11. Same as Fig. 10 except for SWCF.

China Sea and the tropical western Pacific. Between 10°N and 25°N, CRF is not strong until May, but CRF becomes stronger with the onset of the rainy season. In early May, the LWCF exceeds 65 W m^{-2} and the strongest SWCF is less than −70 W m^{-2}. As the rainfall progresses, the strong center of CRF evolves northward, then weakens and withdraws southward, following the evolution of the rainy season. Another belt lies to the east of the TP north of 25°N, particularly between 25°–40°N. After February, there persists strong LWCF and SWCF until May, when there early spring rain begins in South China. The early spring is closely related to dynamic and thermal conditions affected by the TP (Wu et al., 2007). After the rainy season breaks, CRF begins to strengthen and migrate northward. Over East Asia, it is noted that the strongest LWCF appears in the tropical region before the rainy season, but the strongest SWCF lies to the

east of the TP in spring and during the early rainy season.

As shown in Figs. and 11, most models can capture the CRF features in the annual cycle in the tropical regions, and the simulated CRF is also closely related to the simulated rain processes (figure not shown). Nevertheless, compared with the ERBE data, the biases of CRF are very large and the simulated SWCF is too strong after the rainy season. Over the region to the east of the TP, though models simulate well the northward migration of CRF with rainfall, only a couple of models well reproduce the strong SWCF between February and March. Comparatively, GISS-ER captures well the variations of CRF, especially LWCF, from early spring to the onset of the rainy season, but its simulation of CRF in tropical regions has larger biases. MPI-ECHAM5, UKMO-HadGAM1, and GFDL-CM2.1 reproduce well the CRF features in both the above regions. The MME can reduce the model biases partially, and produce a better CRF in tropical regions than most individual models. Meanwhile, the MME can reproduce SWCF and its northward migration. However, the MME still underestimated the strong CRF, and particularly SWCF to the east of the TP between February and March.

6. Discussion and summary

6.1 *Discussion*

There is very complicated topography and air-land-sea interaction in the Asian Monsoon region. Meanwhile, monsoon flow and precipitation are affected by tropical climate systems such as ENSO. Eurasian snow cover and vegetation also have impacts on the monsoon system. Increasing aerosol, particularly absorbing aerosol, and greenhouse gases further modify the monsoon climate (Webster et al., 1998; Meehl, 2007). In addition, topography and the regional climate system have significant differences between South Asia, East Asia, the Maritime Continent, and the western Pacific. All of these factors bring great difficulty and uncertainty for climate simulation in the Asian monsoon region. The same simulation difficulties also appear in the aspect of cloud physics processes.

In our study, qualitative and quantitative analysis shows that the major features of CRF, particularly SWCF, cannot be well reproduced by most IPCC AR4 AMIP models over regions to the east of the TP. Firstly, the simulation biases are tightly associated with the complicated cloud physical processes over the East Asian region. As shown in Figs. 1 and 2, there are a lot of middle-level stratus clouds with large albedo and optical depth that contribute to the strong CRF downstream of the TP (Yu et al., 2004). In fact, the cloud amount (not shown here) also cannot be successfully captured by most IPCC AR4 AMIP models. Apart from cloud amount, CRF is also affected by many other cloud macrophysical and microphysical properties, the simulations of which also have large uncertainties. On the other hand, there exists strong feedback among cloud, radiation, and surface temperature to the east of the TP, where cloud physics processes are affected by large-scale dynamic and thermal conditions (Yu et al., 2004; Li et al., 2005). For such complicated physical processes and their interactions, there are still great challenges for current climate models to realistically reproduce the cloud properties over the East Asian region.

Min et al. (2004) and Jiang et al. (2005) evaluated the surface temperature, sea-level pressure, and precipitation from the IPCC TAR SRES and showed that GFDL_R30_c, ECHAM4/OPYC3, and HadCM3 have better performance. Zhou and Yu (2006) indicated that GFDL-CM2.1 and UKMO-HadGEM1 simulate well the variation of the twentieth-century surface air temperature over East China among the 19 coupled models included in IPCC AR4. Our study also indicates that GFDL-CM2.1, UKMO-HadGAM1, and MPI-ECHAM5 have better performance in CRF simulation over relevant regions. These studies further suggest that improved performance on climatology, including the wind field, temperature, and precipitation, will help CRF simulation downstream of the TP. Hence, it is crucial to ameliorate issues with cloud physical processes of models by better simulation of basic climatology to the east of the TP.

Second, the spatial patterns of the observational and simulated CRF have good correlation with that of the corresponding precipitation, and so do their biases in active convective regions of the Asian monsoon. Meanwhile, the annual cycle of CRF from AMIP models is very close to that of their precipitation over the western Pacific, the South China Sea, and the Maritime Continent, and their biases track closely as well. In the above regions, there exist strong air-sea interactions and cumulus convective processes. In general, the simulated precipitation in active convective regions is directly associated with the cumulus parameterization in models. Cumulus processes change the vertical distribution of temperature and moisture, and also affect the cloud amount, cloud water content, and temperature at cloud top. In this way, cumulus processes influence CRF (Zhang and Mu, 2005). So the larger biases of AMIP models in active convective regions are very likely related to the poor cumulus parameterizations in models.

Current AMIP models are forced by observed SST, which neglects the atmospheric feedback on SST

and leads to improper cumulus convective processes in active convective regions. The coupled ocean-atmosphere processes are extremely important in the heavy precipitation monsoon regions. Many studies (Wang et al., 2004, 2005) have suggested that AGCMs are unable to simulate properly Asian-Pacific summer monsoon rainfall, but AOGCMs have better performance in simulation of rainfall, SST, and their variabilities in summer monsoon regions. Our results further indeed show that the coupled models from IPCC AR4 20CM3 can more reasonably capture the features of rainfall and CRF over the western Pacific, South China Sea, Maritime Continent, and Bay of Bengal (not shown here). However, the coupled models still cannot accurately reproduce the CRF features to the east of the TP, where complicated cloud physics processes bring great difficulty to current climate models. Hence, it is suggested that the proper cloud physical parameterization and a well simulated dynamic structure related to the TP are crucial elements to CRF simulation in the Asian monsoon region.

6.2 *Conclusion*

We have analyzed CRF features in the Asian monsoon region from IPCC AR4 AMIP models. The major results are summarized as follows. In DJF, many models can reproduce the weak CRF between the Indian Peninsula and the Bay of Bengal; only 4 models (MPI-ECHAM5, UKMO-HadGAM1, MRI-CGCM2.3.2, and GISS-ER) of the 10 AMIP models capture the strong SWCF to the east of the TP and no model realistically reproduce the strong LWCF over the TP. In JJA, most models perform well in simulating the major spatial patterns of CRF. However, compared with observations, there appear larger biases for the central location and intensity of simulated CRF in active convective regions, particularly over the Bay of Bengal, where the CRF biases are well correlated with precipitation biases in the models.

Quantitative analysis shows that the CRF terms in AMIP models have large biases and their correlations with observations are not high; the biases of SWCF are larger than that for LWCF and the correlation of SWCF with ERBE is less than 0.8 in JJA. In addition, there also exists large diversity in simulated CRF among models, and the diversity in SWCF is also larger than that for LWCF. As a whole, GFDL-CM2.1, MPI- ECHAM5, UKMO-HadGAM1, and MIROC3.2 (medres) perform well for CRF simulation. Moreover, some models show large differences between DJF and JJA, such as LWCF from CNRM-CM3 and SWCF from MRI-CGCM2.3.2. Additionally, the MME has substantially better CRF values than individual models.

The annual cycle of CRF around East Asia simulated by IPCC AR4 models (0°–50°N, 100°–145°E) is also examined. Though there are biases in the intensity of CRF, most models could capture the basic trends of the annual cycle in the tropical areas (south of 20°N). However, the stronger LWCF and the strongest SWCF from the early spring over the regions to the east of the TP are underestimated by most models. Only GISS-ER, UKMO-HadGAM1, MPI-OM/ECHAM5, and GFDL-CM2.1 perform better in simulating the CRF features over regions to the east of the TP. It is shown in our study that the major regions of bias are located on the lee slide of the TP in DJF and JJA, and in active convective regions in JJA. There are still difficulties faced in simulating CRF in the Asian Monsoon region.

Acknowledgements. This work is jointly supported by the CAS project under Grant No. KZCX2-YW-Q11-01, the Major State Basic Research Development Program of China under Grant No. 2006CB403607 and the National Natural Science Foundation of China (Grant Nos. 40523001, 40821092, 40875034).

REFERENCES

Alekseev, V. A., E. M. Volodin, V. Galin V., V. P. Dymnikov, and V. N. Lykossov, 1998: Modelling of the present-day climate by the INM RAS atmospheric model "DNM GCM". Institute of Numerical Mathematics, Moscow, Russia, 200pp.

Barkstrom, B. R., E. Harrison, G. Smith, R. Green, J. Kibler, R. Cess, and ERBE Science Team, 1989: The Earth Radiation Budget Experiment (ERBE) archival and April 1985 results. *Bull. Amer. Meteor. Soc.*, **70**, 1254–1262.

Chen, G. T.-J., 1994: Large-scale circulations associated with the East Asian summer monsoon and the Mei-Yu over south China and Taiwan. *J. Meteor. Soc. Japan*, **72**, 959–983.

Collins, W. D., and Coauthors, 2004: Description of the NCAR Community Atmosphere Model (CAM3.0). Technical Note TN-464+STR, National Center for Atmospheric Research, Boulder, CO, 214pp.

Déqueé, M., C. Dreveton, A. Braun, and D. Cariolle, 1994: The ARPEGE/IFS atmosphere model: A contribution to the French community climate modeling. *Climate Dyn.*, **10**, 249–266.

Ding, Y. H., 1992: Summer monsoon rainfalls in China. *J. Meteor. Soc. Japan*, **70**, 397–421.

Galin, V. Y., E. M. Volodin, and S. P. Smyshliaev, 2003: Atmospheric general circulation model of INM RAS with ozone dynamics. *Russ. Meteorol. Hydrol.*, **5**, 13–22.

GFDL GAMDT (The GFDL Global Atmospheric Model Development Team), 2004: The new GFDL global atmosphere and land model AM2-LM2: Evaluation

with prescribed SST simulations. *J. Climate*, **17**, 4641–4673.

Giorgi, F., and L. O. Mearns, 2002: Calculation of average, uncertainty range, and reliability of regional climate changes from AOGCM simulations via the "Reliability Ensemble Averaging" (REA) method. *J. Climate*, **15**, 1141–1158.

Hartmann, D. L., M. E. Ockert-Bell, and M. L. Michelson, 1992: The effect of cloud type on earth's energy balance: Global analysis. *J. Climate*, **5**, 1281–1304.

Hourdin, F., and Coauthors, 2006: The LMDZ4 general circulation model: Climate performance and sensitivity to parameterized physics with emphasis on tropical convection. *Climate Dyn.*, **27**, 787–813.

Jiang, D. B., H. J. Wang, and X. M. Lang, 2005: Evalution of East Asian climatology as simulated by seven coupled models. *Adv. Atmos. Sci.*, **22**, 479–495.

K-1 Model Developers, 2004: K-1 Coupled Model (MIROC) Description. K-1 Technical Report 1, H. Hasumi, and S. Emori Eds., Center for Climate System Research, University of Tokyo, Tokyo, Japan, 34pp. [Availableon line from http://www.ccsr.u-tokyo.ac.jp/kyosei/hasumi/MIROC/tech-repo.pdf].

Kiehl, J. T., 1994: On the observed near cancellation between longwave and shortwave cloud forcing in tropical regions. *J. Climate*, **17**, 559–565.

Kiehl, J. T., and V. Ramanathan, 1990: Comparison of cloud radiative forcing derived from the Earth Radiation Budget Experiment with that simulated by the NCAR communityc limate model. *J. Geophys. Res.*, **95**, 11679–11698.

Lau, K. M., M. K. Kim, and K. M. Kim, 2006: Asian summer monsoon anomalies induced by aerosol direct forcing: the role of the Tibetan Plateau. *Climate Dyn.*, **26**, 855–864.

Li, J., R. C. Yu, T. J. Zhou, and B. Wang, 2005: Why is there an early Spring cooling shift downstream of the Tibetan Plateau. *J. Climate*, **18**, 4660–4668.

Liou, K. N., 2004: *An introduction to Atmospheric Radiation*. 2nd ed., China Meteorological Press, Beijing, 612pp. (in Chinese)

Martin, G. M., and Coauthors, 2004: Evaluation of the atmospheric performance of HadGAM/GEM1. Hadley Centre Technical Note, No. 54, Hadley Centre for Climate Prediction and Research/Met Office, Exeter, UK. [Availableon line from http://www. metoffice.gov.uk/research/hadleycentre/pubs/HCTN/ ind ex.html].

Ma, X. Y., and G. L. Ji, 2000: Analysis of temporal and spacial variations for cloud radiative forcing in China by using ERBE data. *Plateau Meteorology*, **19**, 150–158. (in Chinese)

Meehl, G. A., and Coauthors, 2007: Global climate projections. *Climate Change 2007: The Physical Science Basis. Contribution of Working Group I to the Fourth Assessment Report of the Intergovernmental Panel on Climate Change*, S. Solomon et al., Eds., Cambridge University Press, Cambridge, United Kingdom and New York, NY, USA.

Min, S. K., E. H. Park, and W. T. Kwon, 2004: Future projections of East Asian climate change from multi-AOGCM ensembles of IPCC SRES scenario simulations. *J. Meteor. Soc. Japan*, **82**, 1187–1211.

Rajeevan, M., and J. Srinivasan, 2000: Net cloud radiative forcing at the top of the atmosphere in the Asian Monsoon region. *J. Climate*, **13**, 650–657.

Ramanathan, V., R. D. Cess, E. F. Harrison, P. Minnis, B. R. Barkstrom, E. Ahmad, and D. Hartmann, 1989: Cloud-radiative forcing and climate: Results from the Earth Radiation Budget Experiment. *Science*, **243**, 57–63.

Raschke E., A. Ohmura, W. B. Rossow, B. E. Carlson, Y. C. Zhang, C. Stubenrauch, M. Kottek, and M. Wild, 2005: Cloud effects on the radiation budget based on ISCCP data (1991–1995). *International Journal of Climatology*, **25**, 1103–1125.

Roeckner, E., G. Bauml, L. Bonaventura, R. Brokopf, and M. Esch, 2003: The atmospheric general circulation model ECHAM5. Part I: Model description. MPI Report, No. 349, Max Planck Institute für Meteorology, Hamburg, Germany, 127pp.

Rossow, W. B., and R. A. Schiffer, 1999: Advances in understanding clouds from ISCCP. *Bull. Amer. Meteor. Soc.*, **80**, 2261–2287.

Schmidt, G. A., and Coauthors, 2006: Present day atmospheric simulations using GISS ModelE: Comparison to in-situ, satellite and reanalysis data. *J. Climate*, **19**, 153–192.

Shi, G. Y., 2007: *Atmospheric Radiation*. Science Press, Beijing, 402pp. (in Chinese)

Shibata, K., H. Yoshimura, M. Ohizumi, M. Hosaka, and M. Sugi, 1999: A simulation of troposphere, stratosphere and mesosphere with an MRI/JMA98 GCM. *Papers in Meteorology and Geophysics*, **50**, 15–53.

Stephens, G. L., 2005: Cloud feedbacks in the climate system: A critical review. *J. Climate*, **18**, 237–273.

Sun, Z. A., 1995: Comparison of observed and modelled radiation budget over the Tibetan Plateau using satellite data. *International Journal of Climatology*, **15**, 423–445.

Taylor, K. E., 2001: Summarizing multiple aspects of model performance in a single diagram. *J. Geophys. Res.*, **106**, 7183–7192.

Wang, B., and H. Lin, 2002: Rainy season of the Asian-Pacific summer monsoon. *J. Climate*, **15**, 386–398.

Wang, B., I. S. Kang, and J. Y. Lee, 2004: Ensemble simulations of Asian-Australian monsoon variability by 11 AGCMs. *J. Climate*, **17**, 803–818.

Wang, B., Q. H. Ding, X. H. Fu, I. S. Kang, K. Jin, J. Shukla, and F. Doblas-Reyes, 2005: Fundamental challenge in simulation and prediction of summer monsoon rainfall. *Geophys. Res. Lett.*, **32**, L15711, doi:10.1029/2005GL022734.

Webster, P. J., V. O. Magana, T. N. Palmer, J. Shukla, R. A. Tomas, M. Yanai, and T. Yasunari, 1998: Monsoons: Processes, predictability, and the prospects for prediction, *J. Geophys. Res.*, **103**, 14451–14510.

Wu, G. X., and Coauthors, 2007: The influence of the me-

chanical and thermal forcing of the Tibetan Plateau on the Asian climate. *Journal of Hydrometeorology*, **8**, 770–789.

Xie, P. P., and P. A. Arkin, 1997: Global precipitation: A 17-year monthly analysis based on gauge observation, satellite estimates, and numerical model outputs. *Bull. Amer. Meteor. Soc.*, **78**, 2539–2558.

Yu, R. C., Y. Q. Yu, and M. H. Zhang, 2001: Comparing cloud radiative properties between the eastern China and the Indian monsoon region. *Adv. Atmos. Sci.*, **18**, 1090–1102.

Yu, R. C., B. Wang, and T. J. Zhou, 2004: Climate effects of the deep continental stratus clouds generated by the Tibetan Plateau. *J. Climate*, **17**, 2702–2713.

Zhang, G. J., and M. Q. Mu, 2005: Effects of modifications to the Zhang-McFarlane convection parameterization on the simulation of the tropical precipitation in the National Center for Atmospheric Research Community Climate Model, version 3. *J. Geophys. Res.*, **110**, D09109, doi:10.1029/2004JD005617.

Zhou, T. J., and R. C. Yu, 2006: 20th century surface air temperature over China and the globe simulated by coupled climate models. *J. Climate*, **19**, 5843–5858.